

A two-dimensional optomechanical crystal for quantum transduction

Felix M. Mayor,^{1,*} Sultan Malik,^{1,*} André G. Primo,^{1,2,*} Samuel Gyger,^{1,*}
Wentao Jiang,¹ Thiago P. M. Alegre,² and Amir H. Safavi-Naeini^{1,†}

¹*Department of Applied Physics and Ginzton Laboratory,*

Stanford University, 348 Via Pueblo Mall, Stanford, California 94305, USA

²*Gleb Wataghin Institute of Physics, University of Campinas, 13083-859 Campinas, SP, Brazil*

(Dated: June 21, 2024)

Integrated optomechanical systems are one of the leading platforms for manipulating, sensing, and distributing quantum information. The temperature increase due to residual optical absorption sets the ultimate limit on performance for these applications. In this work, we demonstrate a two-dimensional optomechanical crystal geometry, named **b-dagger**, that alleviates this problem through increased thermal anchoring to the surrounding material. Our mechanical mode operates at 7.4 GHz, well within the operation range of standard cryogenic microwave hardware and piezoelectric transducers. The enhanced thermalization combined with the large optomechanical coupling rates, $g_0/2\pi \approx 880$ kHz, and high optical quality factors, $Q_{\text{opt}} = 2.4 \times 10^5$, enables the ground-state cooling of the acoustic mode to phononic occupancies as low as $n_m = 0.35$ from an initial temperature of 3 K, as well as entering the optomechanical strong-coupling regime. Finally, we perform pulsed sideband asymmetry of our devices at a temperature below 10 mK and demonstrate ground-state operation ($n_m < 0.45$) for repetition rates as high as 3 MHz. Our results extend the boundaries of optomechanical system capabilities and establish a robust foundation for the next generation of microwave-to-optical transducers with entanglement rates overcoming the decoherence rates of state-of-the-art superconducting qubits.

The integration of mechanical systems with photonic circuits [1] offers a versatile platform for high-performance sensors [2], signal processing [3] and exploring macroscopic systems in the quantum regime [4]. These optomechanical devices [5] allow for precise detection of motion using light at and beyond the standard quantum limit [6], enabling the measurement of acceleration [7], displacement [8], mass [9], forces [10] at both room and cryogenic temperatures, and the transduction of quantum information between disparate energy scales [11, 12].

Silicon-based optomechanical crystals (OMC) [13] are particularly promising systems with exceptional photon-phonon cooperativity. This is due to their high optical and mechanical quality factors combined with large optomechanical couplings, enabled by their sub-wavelength modal volumes. Their operation at the quantum level is possible using either milli-Kelvin cryogenic environments or by laser cooling the mechanical modes into their ground state from precooled conditions [14]. This enables the preparation of mechanical quantum states [15], optical squeezed states [16], as well as the demonstration of entanglement between mechanical resonators [17]. The availability of high-frequency mechanical modes in the GHz regime, combined with piezoelectric [18, 19] or electrostatic coupling [20], make these structures ideal for coherently transducing quantum signals from the microwave to the optical domain to build superconducting qubits-based quantum networks [21].

OMCs are typically nanobeams patterned along one-

dimension (1D) [22] (≈ 500 nm in width) that are released from the substrate and co-confine optical and mechanical modes. In such devices, heat only dissipates to the surrounding material along the length of the beam. The residual heating through linear and non-linear absorption [23, 24], leads to resonance shifts and optical instabilities at room temperature [25], while at cryogenic temperatures heating of the mechanical mode hinders operation in the quantum limit. Therefore various strategies are being pursued to improve thermalization and minimize residual heating. First, utilizing non-suspended OMCs may help with thermal anchoring [26] as the heat can propagate into the bulk of the chip. Second, cooling the device using a buffer gas, as demonstrated with ³He at ≈ 2 K [27] has been effective at maintaining low temperatures while laser driving. However, immersion in liquid ⁴He, which transitions to a superfluid below 2.17 K, introduces new and interesting superfluid-structure interactions and dynamics which seem to complicate operating the device as a transducer [28, 29].

One approach to reducing the challenges posed by heating is to develop two-dimensional (2D) OMCs [30–32]. The initial demonstrations of these devices had limited coupling rates and a complicated mechanical mode spectrum, which largely negated their purported benefits in thermalization. A major advance in 2D OMC design [31] led to photon-phonon coupling rates on par with their 1D counterparts while demonstrating improved thermalization in continuous-wave (CW) operation. Nonetheless, 2D OMCs are yet to be incorporated into optomechanical transducers. Part of the challenge is due to their generally higher microwave operating frequency – more than 10 GHz vs. less than 5 GHz for 1D OMCs. This is because fully connected 2D structures

* These authors contributed equally

† safavi@stanford.edu

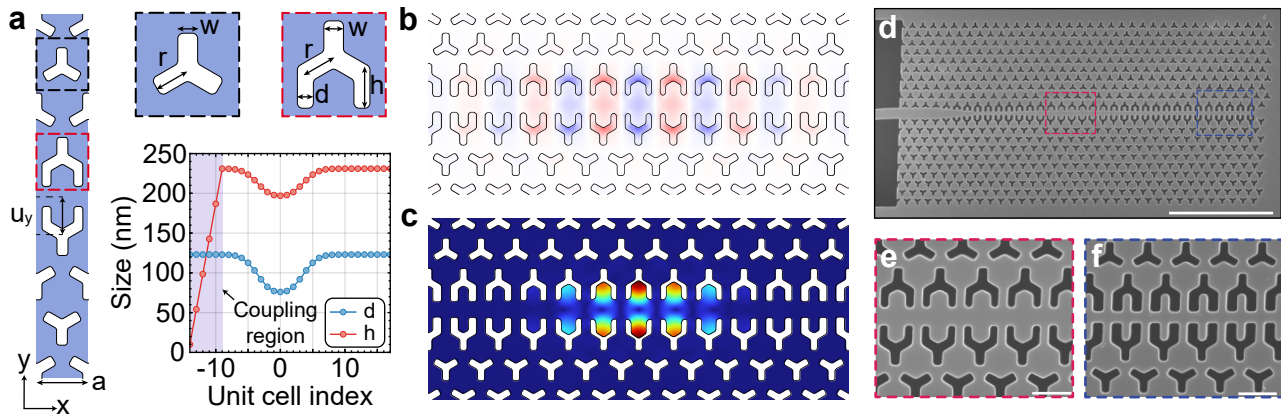


FIG. 1. **2D Optomechanical crystal design and implementation.** **a**, Schematic of the waveguide unit cell and definition of parameters. Typical parameters are $a = 448$ nm, $w = 93$ nm, $r = 172$ nm and a fillet radius of 25 nm. The dimensions d and h are modified along the length of the waveguide to confine the optical and acoustic fields. To couple light into the cavity, h is linearly tapered down. **b**, **c** FEM simulations of the full cavity displaying the electric field E_y of the fundamental optical mode and the displacement profile of the mechanical mode of interest. **d**, Scanning electron micrograph of the fabricated optomechanical crystal. Scale bar is 5 μm . **e**, **f** Close-up of the defect and mirror regions of the waveguide. Scale bars are 500 nm.

are generally stiffer than 1D devices. Higher operation frequency makes piezoelectric coupling to the mode more difficult, requires a higher optical driving power due to a larger sideband detuning, and leads to a mismatch in frequency with most superconducting qubit systems that tend to operate on the 4 to 8 GHz range. Secondly, integrated optomechanical transducers have mostly operated as optically pulsed devices to avoid issues related to heating dynamics which kick in on a slower time scale than the pulse duration. It is therefore important to demonstrate the advantages of the 2D OMCs while operating them in optically pulsed mode.

Here we present a novel Si-based two-dimensional OMC with high optical and mechanical quality factors. In contrast to prior demonstrations, the device operates within the typical superconducting qubit frequency band and allows for straightforward integration with a piezoelectric transducer [18, 33, 34]. The enhanced thermalization allows us to demonstrate ground-state side-band cooling by CW optical driving starting from a fridge temperature of ≈ 3 K. Moreover, due to improved power handling, the device operates in a stable manner at sufficiently high power to achieve continuous strong coupling between the optical and mechanical modes – a first for silicon optomechanical devices to our knowledge. We demonstrate pulsed operation at < 10 mK at repetition rates as large as 3 MHz with the mechanical mode occupation still in the ground state. Our findings provide a pathway to high-repetition entanglement creation utilizing optomechanical transducers [35–37].

I. RESULTS

A. Two-dimensional C-band optomechanical crystal

Our Si-based two-dimensional OMC is built on a hybrid **b-dagger** (*boomerang-dagger*) design, where the optomechanical shield is based on the *boomerang* unit-cell (identical to the *blade* cell proposed in Ref. [38]) and the defect region is designed in a *dagger* shape. Fig. 1a depicts a schematic of the effective waveguide unit cell of the device together with the parameters defining our design. We align the x -axis of our device along the $[1, 0, 0]$ crystal orientation of silicon, where the stiffness coefficients are lower resulting in lower mechanical frequencies [39]. Optomechanical confinement is achieved by adiabatically modifying the dagger parameters d and h as shown in Fig. 1a such as to locally create a density of states inside the photonic and phononic bandgaps (see Supplementary Figure 2). We use finite element method (FEM) simulations combined with particle swarm optimization to simultaneously optimize the optical and mechanical quality factors, Q_{opt} and Q_{m} , and the single-photon optomechanical coupling rate g_0 while minimizing the mechanical frequency ω_{m} . The mode profiles of interest are displayed in Fig. 1b and c, showing wavelength-scale confinement in both the optical and acoustic domains. Our devices operate at an optical frequency $\omega_c/2\pi \approx 193$ THz, well within the telecom C-band, at $\omega_{\text{m}}/2\pi \approx 7.5$ GHz, with radiation-limited $Q_{\text{opt}} > 5 \times 10^6$ and $Q_{\text{m}} > 1 \times 10^9$. We compute the optimal g_0 accounting for both moving boundary and photoelastic contributions [40], yielding $g_0/2\pi \approx 950$ kHz. The fabricated device (see Methods) is shown in the scanning electron micrograph in Fig. 1d with a close-up of the center defect

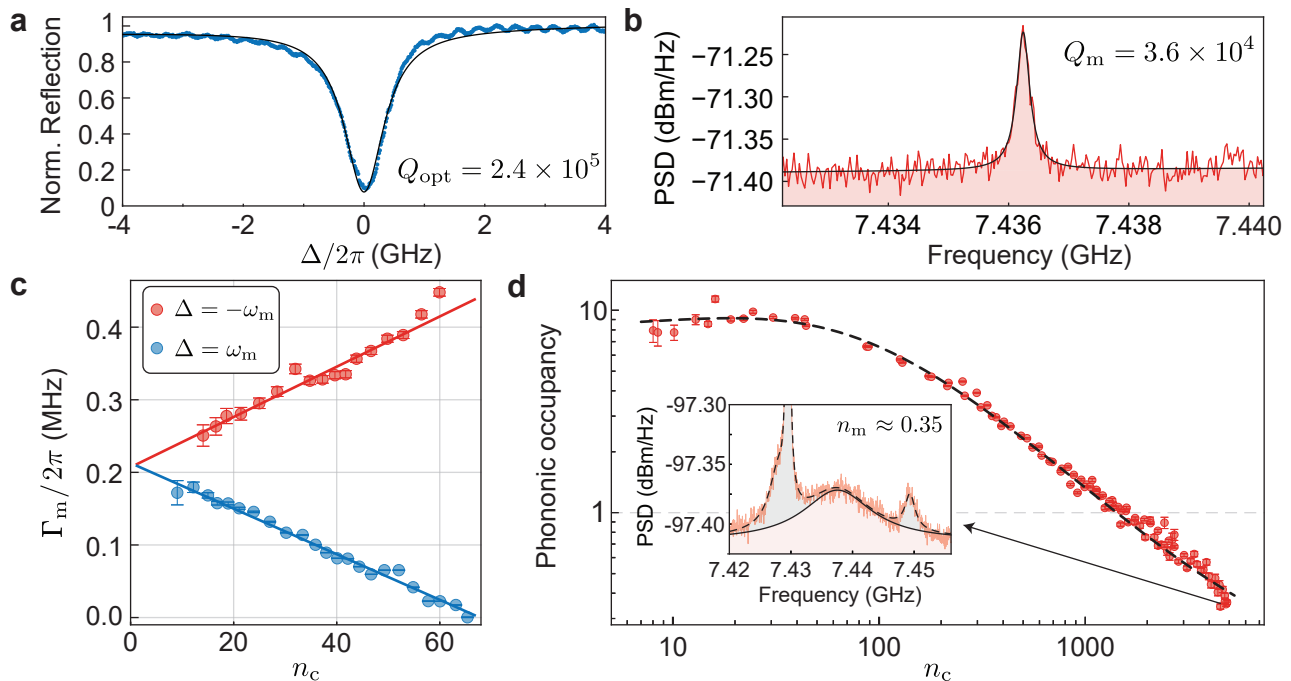


FIG. 2. **Ground-state cooling of the mechanical mode.** **a**, Room temperature optical spectrum as function of the laser-cavity detuning $\Delta = \omega_1 - \omega_c$. **b**, Mechanical response of the OMC at $T = 3$ K. **c**, Backaction cooling and amplification as a function of photon number (n_c), under both red- and blue-detuned excitation. **d**, Ground state cooling of the mechanical mode. Inset: mechanical spectrum for the highest intracavity occupation in the experiment, $n_c \approx 4800$. The error bars represent one standard deviation around the fit value.

and mirror in Fig. 1e and Fig. 1f respectively.

We study the devices at room temperature, 3 K, and 10 mK. The cryogenic measurements were done at the mixing chamber plate of a dilution refrigerator before and after condensation. We measure the room-temperature optical response using a lensed fiber to send and collect light from an on-chip waveguide butt-coupled to the b-dagger OMC. A typical reflection spectrum is shown in Fig. 2a displaying the fundamental optical mode at $\omega_c/2\pi = 191.7$ THz (1563.5 nm) as a function of the laser-cavity detuning $\Delta = \omega_1 - \omega_c$. A Lorentzian fit to the data yields a loaded $Q_{\text{opt}} = 2.4 \times 10^5$ (2.2×10^5 at 3 K), with an extrinsic coupling rate $\kappa_e/2\pi \approx 288$ MHz (measured through coherent sideband spectroscopy), putting the device close to critical coupling. The mechanical spectrum at $T = 3$ K is assessed through amplitude fluctuations imparted on the reflected optical signal by the thermo-mechanical motion of the OMC. This signal is then measured using a high-speed photodetector and a real-time spectrum analyzer yielding the photocurrent power spectral density (PSD). The mechanical breathing mode of the OMC is found at $\omega_m/2\pi \approx 7.436$ GHz with $Q_m = 3.6 \times 10^4$ as shown in Fig. 2b.

Our device operates well within the sideband-resolved regime $\omega_m > \kappa$ ($\kappa/2\pi \approx 800$ MHz). In this regime, the linearized optomechanical interaction under a blue-detuned, $\Delta = \omega_m$ (red-detuned, $\Delta = -\omega_m$), coherent excitation is reduced to a two-mode squeezing (beam-

splitter) interaction, with Hamiltonian $\hat{H} = \hbar g(\hat{a}\hat{b} + \hat{a}^\dagger\hat{b}^\dagger)$ ($\hat{H} = \hbar g(\hat{a}\hat{b}^\dagger + \hat{a}^\dagger\hat{b})$) [41]. This interaction leads to the mechanical mode's effective amplification (cooling), associated with a narrowing (broadening) of its linewidth. Here, $g = g_0\sqrt{n_c}$ is the linearized effective optomechanical coupling, enhanced by the number of photons circulating in the cavity, n_c , and \hat{a} , \hat{b} denote the annihilation operators for photons and phonons, respectively.

In Fig. 2c we characterize the mechanical linewidth, Γ_m , as a function of n_c , for both red- ($\Delta < 0$) and blue-detuned ($\Delta > 0$) excitation. In the sideband-resolved regime, $\Gamma_m \approx \Gamma_m^0(1 + C)$, where $C = 4g_0^2 n_c / (\kappa \Gamma_m^0)$ is the optomechanical cooperativity and Γ_m^0 is the bare mechanical linewidth. A linear fit to the measured data yields $g_0/2\pi = 901(3)$ kHz ($\Delta = -\omega_m$) and $g_0/2\pi = 860(1)$ kHz ($\Delta = \omega_m$), in good agreement with simulation results. We attribute the discrepancy found for the values of g_0 under red and blue excitation to uncertainty in the cavity occupation arising from the Fano lineshape of the optical resonance and variations in the fiber-to-cavity coupling efficiency for different excitation frequencies.

B. Ground-state cooling of the mechanical mode

A mechanical resonator placed at a temperature $T \ll \hbar\omega/k_B$, will occupy its ground state nearly perfectly. For a 7 GHz resonator this condition is achieved at the 10 mK

temperature base temperature of dilution refrigerators. Operating at such low temperatures poses many challenges largely rooted in the extremely small (microwatt-level) available cooling powers, vanishing heat capacity, and small thermal couplings. It is therefore important to consider whether quantum operation is possible at higher temperatures where less exotic cryogenic systems provide orders of magnitude greater cooling power, making scaling to more transducers and control lines more realistic. Higher temperature has been previously considered as a route to improved microwave-to-optical transducers [27, 36, 42]. The first demonstration of optical ground state cooling started from a temperature of roughly $T_{\text{ini}} = 20$ K [14]. Rather counter-intuitively, for silicon optomechanical devices, laser cooling from lower starting temperatures becomes *more* challenging, since the temperature increase due to optical absorption heating grows more quickly as the temperature is reduced than the advantage of starting with a lower initial phonon population [43]. Operation in the quantum regime from a lower starting temperature than 20 K is however important for developing transducers, since the superconducting materials used in such devices will need to have a critical temperature $T_c \gg T_{\text{ini}}$ to avoid excess quasi-particle losses, and for many common materials T_c 's are in the range of 10–15 K.

Starting from a base temperature of 3 K, we laser cool our 2D OMC device into its quantum ground state. In Fig. 2d, we show the inferred mechanical mode occupation as a function of the laser-driven intracavity photon number n_c . The phonon occupancy, n_m , is obtained through the area under the measured thermo-mechanical response of the acoustic mode at 7.436 GHz. In this measurement, we calibrated the photodetection gain for different input powers by intensity modulating the laser at 7.446 GHz and measuring its PSD. The input laser is filtered to mitigate contributions from technical laser noise in the measured mechanical spectrum [44] reducing the maximum excitation power attainable in the experiment. At low optical powers ($n_c < 10$), we assume the acoustic mode is thermalized to the plate temperature of 3 K, with a phononic occupancy $n_m = n_{\text{th}} \approx 7.95$. At high input powers, $n_c \approx 5000$, the effective temperature of the mechanical mode is cooled to $T_{\text{eff}} \approx 260$ mK, yielding $n_m \approx 0.35 \pm 0.01$, corresponding to a 74% probability of ground-state occupation. The black dashed line depicts the theoretical prediction for cooling in the presence of a phenomenological increase in the acoustic thermal bath temperature with n_c (see Methods). In the high intracavity field regime, several modes appear in the mechanical spectra and are included in our fits (see inset of Fig. 2d) for an accurate calibration of n_m .

C. Optomechanical strong coupling

Another straightforward consequence of the better thermal anchoring of two-dimensional optomechanical

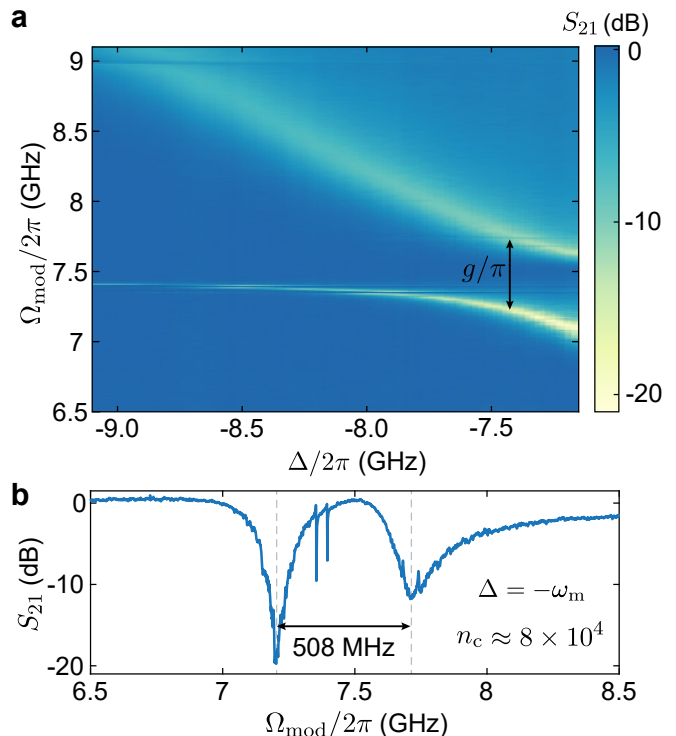


FIG. 3. **Optomechanical strong coupling.** **a**, Measurement of optomechanically-induced transparency (OMIT) as a function of laser detuning Δ . The avoided crossing at $\Omega_{\text{mod}} \approx -\omega_m$ results from the strong coupling between the optical and mechanical mode of the OMC. **b**, Line-cut of **a** at $\Delta = -\omega_m$. From the splitting, we infer that we are in the strong coupling regime ($g/\pi = 508$ MHz $> \kappa/4\pi$). The strong pump field makes additional weakly coupled mechanical modes visible.

crystals is the strong suppression of thermo-optic nonlinearities. The temperature increase in typical devices red-shifts the optical resonance, leading to an unstable optical response for a sufficiently strong red-detuned pump. For 1D OMCs, this effect usually constrains $n_c < 2000$ [45–47] precluding the onset of the strong coupling regime ($4g > \kappa$) [48], where the optical and mechanical modes hybridize, hence enabling the coherent state swap between photonic and phononic domains.

To observe strong coupling, we perform optomechanically induced transparency measurements. We intensity-modulate a pump laser detuned by Δ with respect to the optical mode of the OMC at a frequency Ω_{mod} using an electro-optical modulator and a vector network analyzer. The latter is used to measure the coherent response of the b-dagger OMC, $S_{21}(\Omega_{\text{mod}})$. When $\Omega_{\text{mod}} = \omega_m$, the anti-Stokes sideband arising from the modulation interferes with mechanically-scattered photons giving rise to a transparency window in $|S_{21}|$, indicating a hybridization of mechanical and optical loss channels. We measure this response as a function of the pump detuning Δ (Fig. 3a) for an on-chip pump power of 9.4 mW (corresponding to $n_c \approx 8 \times 10^4$). When the pump is red-detuned by

$\Delta = -\omega_m$, we observe an avoided crossing with a frequency splitting $g/\pi = 508$ MHz (Fig. 3b). From a fit of S_{21} at large detuning $\Delta \approx -9.5$ GHz, we obtain an optical linewidth $\kappa/2\pi = 870$ MHz. This puts our system well into the strong coupling regime ($4g/\kappa \approx 1.17$), so far elusive in wavelength-scale silicon devices.

D. Pulsed sideband thermometry at $T \lesssim 10$ mK

We characterize a second device at $T \lesssim 10$ mK using pulsed sideband asymmetry measurements on the mechanical breathing mode. Fig. 4a shows a simplified measurement setup. Starting with a blue- and a red-detuned laser, both parked and locked one mechanical frequency away from the optical cavity resonance, we use two acousto-optic modulators (AOM) in series to generate optical pulses of length $\tau = 80$ ns with an on-chip peak pump power $P_{\text{peak}} \approx 7.4$ μ W. Through optomechanical interaction, a fraction of the optical pump photons get scattered (or frequency-shifted) into sideband photons resonant with the optical cavity. The reflected light, consisting of residual pump and sideband photons, then passes through a pair of narrowband Fabry-Pérot cavities (bandwidth ≈ 15 MHz) that suppress the pump photons with a joint suppression of > 90 dB with respect to the sideband photons. The transmitted sideband photons are then detected by a superconducting nanowire single-photon detector (SNSPD), and the recorded photon clicks are time-tagged. The photon clicks are averaged over multiple trials of the experiment, interleaved every 20 minutes between the blue- and red-detuned laser. Pulse generation and data acquisition are performed using an FPGA-based real-time controller.

Using the optical pulse parameters and the measured device properties, we estimate the photon-phonon Stokes scattering probability $p_s \approx 4g_0^2 n_c \tau / \kappa \approx 5\%$, calculated assuming the mechanical mode in the ground-state. Fig. 4b shows a time-resolved histogram of the optomechanically scattered sideband photons averaged over millions of experimental runs for blue- and red-detuned lasers for an optical pulse repetition rate of 188 kHz. Dark counts arising from spurious light and detector noise are shown in grey (≈ 5 Hz). The asymmetry between the sideband count rates under blue-detuned operation (proportional to $p_s(n_m + 1)$) and red-detuned operation (proportional to $p_s n_m$) provides a direct way to quantify the thermal occupation of our mechanical mode. The asymmetry in count rates stems from the quantum nature of the processes involved: while transitions to higher phonon states induced by the blue-detuned pump are always possible, phonon annihilation due to the interaction with the red-detuned pump is completely suppressed if the mechanical mode is in the ground state. From the asymmetry measured in Fig. 4b, we extract a phonon occupation $n_m = 0.043 \pm 0.001$.

The pulsed sideband asymmetry measurements are performed for various optical pulse repetition rates, and the resulting phonon occupation is shown in Fig. 4c, revealing the effect of optically-induced heating of the mechanical mode. While the thermal occupation increases with the increasing repetition rate as expected, our device stays in the ground state for a repetition rate as high as 3.012 MHz, with a thermal occupation $n_m = 0.42 \pm 0.02$. Our device demonstrates one of the lowest reported thermal occupations for an OMC under pulsed operation, representing a reduction by roughly a factor of eight in the thermal occupation of the mechanical mode compared to 1D structures at similar repetition rates and photon-phonon scattering probabilities [49, 50].

II. DISCUSSION

In summary, we designed, fabricated, and demonstrated a proof-of-principle experiment for high-rate phonon-photon pair generation without significant residual heating using a silicon-based 2D optomechanical crystal. The enhanced thermal anchoring of our design enables the ground state cooling of the mechanical mode and entering the optomechanical strong coupling regime. These demonstrations open the way for full quantum control of integrated optomechanical systems operated at temperatures of $T \approx 3$ K, routinely reached by Gifford-McMahon cryocoolers, allowing for simplified cryogenic infrastructure for quantum sensing and communication applications. Moreover, the large cooperativity that we achieve ($C > 1000$) enables a new class of experiments where photonic states can be coherently swapped into the mechanical domain and vice versa, leveraging nanomechanical resonators as sources of optical quantum states. Increasing Q_m , which could be achieved by adding more phononic shields to the crystal structure [51], could also propel the use of our mechanical mode as a sensor and as a quantum memory for light. Lastly, our optical quality factors are fabrication-limited and can exceed a few million in similar two-dimensional photonic structures [52, 53]. An enhancement in Q_{opt} would reduce the intracavity field required to achieve moderate scattering probabilities and thus further decrease the thermal phononic occupancy under pulsed excitation.

In a next step, our device can be co-integrated with piezoelectric materials to complete a high-rate conversion chain from microwave to optical photons. For linking two superconducting quantum computing units, the entanglement rate needs to exceed the decoherence rate of local qubits, while at the same time avoiding thermal noise. To ensure continuous entanglement availability in superconducting qubit nodes, the demonstrated excitation rates up to \sim MHz, considering expected microwave and optical efficiencies [18], are enough to exceed the $T_2 = 0.1$ ms of state of the art superconducting qubits.

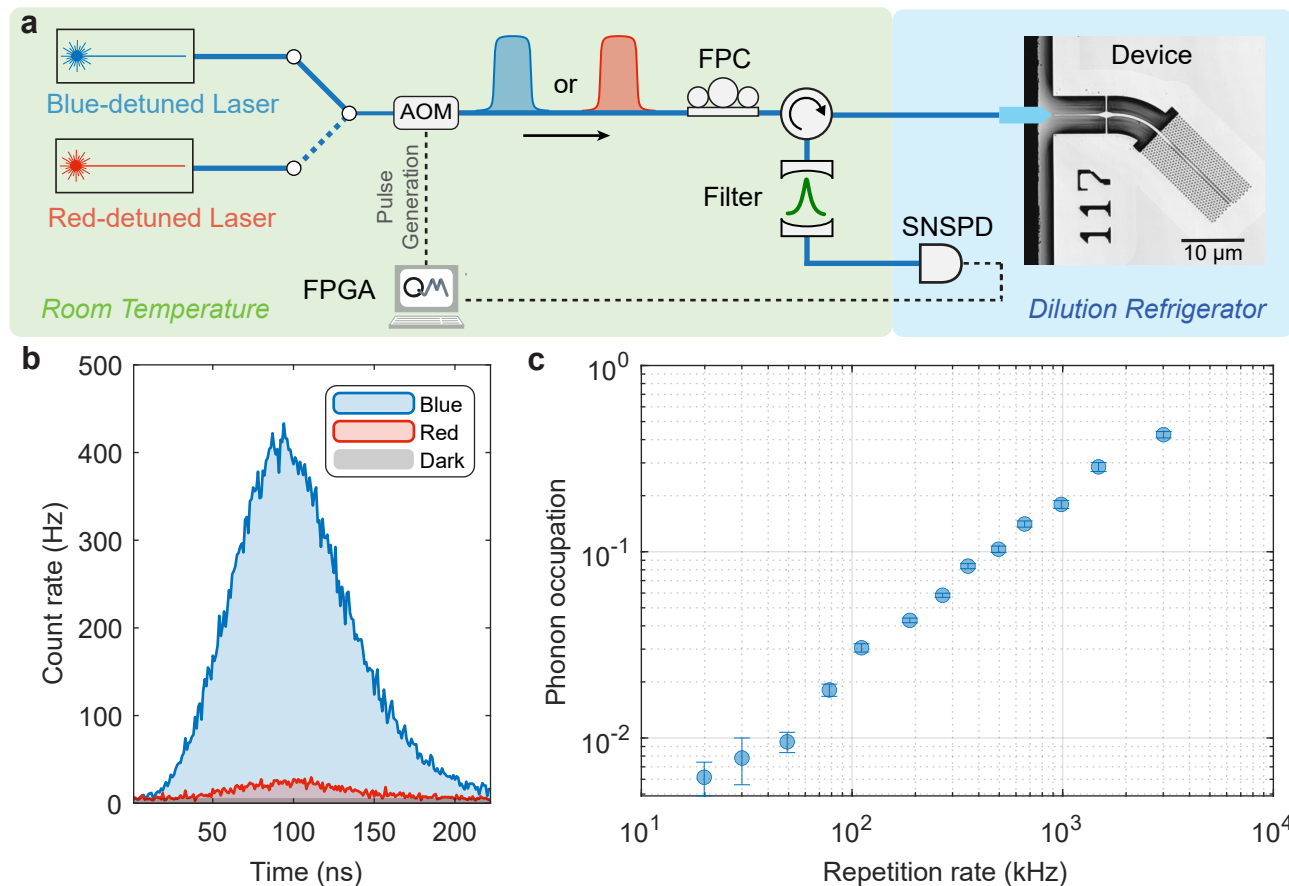


FIG. 4. **Pulsed sideband asymmetry measurement.** **a**, Simplified setup of the pulsed sideband asymmetry measurement with the device at $T \lesssim 10$ mK. Blue- or red-detuned optical pump pulses of length $\tau = 80$ ns incident on the device generate sideband photons on-resonance with the optical cavity. The reflected light, containing residual pump and sideband photons, is filtered to suppress the pump. The transmitted sideband photons are detected with a single photon detector, and the photon clicks are time-tagged. **b**, Time trace of the sideband photons generated using blue- and red-detuned pump pulses for a scattering probability of $\approx 5\%$ and a pulse repetition rate of 188 kHz. From the asymmetry between the blue and red count rates, we extract a phonon occupation of ≈ 0.043 . **c**, Phonon occupation for a scattering probability of $\approx 5\%$ for different pulse repetition rates quantifying the effect of optically-induced heating of the mechanical mode. The error bars represent the standard error over multiple sets of measurements (ranging from 4 to 52 depending on the repetition rate).

- [1] Safavi-Naeini, A. H., Van Thourhout, D., Baets, R. & Van Laer, R. Controlling phonons and photons at the wavelength scale: Integrated photonics meets integrated photonics. *Optica* **6**, 213–232 (2019).
- [2] Li, B.-B., Ou, L., Lei, Y. & Liu, Y.-C. Cavity optomechanical sensing. *Nanophotonics* **10**, 2799–2832 (2021).
- [3] Eggleton, B. J., Poulton, C. G., Rakich, P. T., Steel, M. J. & Bahl, G. Brillouin integrated photonics. *Nature Photonics* **13**, 664–677 (2019).
- [4] Barzanjeh, S. *et al.* Optomechanics for quantum technologies. *Nature Physics* **18**, 15–24 (2022).
- [5] Aspelmeyer, M., Kippenberg, T. J. & Marquardt, F. Cavity optomechanics. *Reviews of Modern Physics* **86**, 1391–1452 (2014).
- [6] Mason, D., Chen, J., Rossi, M., Tsaturyan, Y. & Schliesser, A. Continuous force and displacement measurement below the standard quantum limit. *Nature Physics* **15**, 745–749 (2019).
- [7] Krause, A. G., Winger, M., Blasius, T. D., Lin, Q. & Painter, O. A high-resolution microchip optomechanical accelerometer. *Nature Photonics* **6**, 768–772 (2012).
- [8] Eichenfield, M., Camacho, R., Chan, J., Vahala, K. J. & Painter, O. A picogram- and nanometre-scale photonic-crystal optomechanical cavity. *Nature* **459**, 550–555 (2009).
- [9] Sansa, M. *et al.* Optomechanical mass spectrometry. *Nature Communications* **11**, 3781 (2020).
- [10] Gavartin, E., Verlot, P. & Kippenberg, T. J. A hybrid on-chip optomechanical transducer for ultrasensitive force measurements. *Nature Nanotechnology* **7**, 509–514 (2012).
- [11] Andrews, R. W. *et al.* Bidirectional and efficient conversion between microwave and optical light. *Nature Physics* **10**, 321–326 (2014).

- [12] Forsch, M. *et al.* Microwave-to-optics conversion using a mechanical oscillator in its quantum ground state. *Nature Physics* **16**, 69–74 (2020).
- [13] Eichenfield, M., Chan, J., Camacho, R. M., Vahala, K. J. & Painter, O. Optomechanical crystals. *Nature* **462**, 78–82 (2009).
- [14] Chan, J. *et al.* Laser cooling of a nanomechanical oscillator into its quantum ground state. *Nature* **478**, 89–92 (2011).
- [15] Riedinger, R. *et al.* Non-classical correlations between single photons and phonons from a mechanical oscillator. *Nature* **530**, 313–316 (2016).
- [16] Safavi-Naeini, A. H. *et al.* Squeezed light from a silicon micromechanical resonator. *Nature* **500**, 185–189 (2013).
- [17] Riedinger, R. *et al.* Remote quantum entanglement between two micromechanical oscillators. *Nature* **556**, 473–477 (2018).
- [18] Jiang, W. *et al.* Optically heralded microwave photon addition. *Nature Physics* **19**, 1423–1428 (2023).
- [19] Meesala, S. *et al.* Non-classical microwave–optical photon pair generation with a chip-scale transducer. *Nature Physics* 1–7 (2024).
- [20] Zhao, H., Bozkurt, A. & Mirhosseini, M. Electro-optic transduction in silicon via gigahertz-frequency nanomechanics. *Optica* **10**, 790–796 (2023).
- [21] Han, X., Fu, W., Zou, C.-L., Jiang, L. & Tang, H. X. Microwave-optical quantum frequency conversion. *Optica* **8**, 1050–1064 (2021).
- [22] Chan, J., Safavi-Naeini, A. H., Hill, J. T., Meenehan, S. & Painter, O. Optimized optomechanical crystal cavity with acoustic radiation shield. *Applied Physics Letters* **101**, 081115 (2012).
- [23] Borselli, M., Johnson, T. J. & Painter, O. Measuring the role of surface chemistry in silicon microphotonic. *Applied Physics Letters* **88**, 131114 (2006).
- [24] Meenehan, S. M. *et al.* Pulsed Excitation Dynamics of an Optomechanical Crystal Resonator near Its Quantum Ground State of Motion. *Physical Review X* **5**, 041002 (2015).
- [25] Cui, K. *et al.* Phonon lasing in a hetero optomechanical crystal cavity. *Photonics Research* **9**, 937–943 (2021).
- [26] Kolvik, J., Burger, P., Frey, J. & Van Laer, R. Clamped and sideband-resolved silicon optomechanical crystals. *Optica* **10**, 913–916 (2023).
- [27] Qiu, L., Shomroni, I., Seidler, P. & Kippenberg, T. J. Laser Cooling of a Nanomechanical Oscillator to Its Zero-Point Energy. *Physical Review Letters* **124**, 173601 (2020).
- [28] Korsch, A. R., Fiaschi, N. & Gröblacher, S. Phononic Crystals in Superfluid Thin-Film Helium (2024). 2402.18259.
- [29] Sachkou, Y. P. *et al.* Coherent vortex dynamics in a strongly interacting superfluid on a silicon chip. *Science* **366**, 1480–1485 (2019).
- [30] Safavi-Naeini, A. H. *et al.* Two-Dimensional Phononic-Photonic Band Gap Optomechanical Crystal Cavity. *Physical Review Letters* **112**, 153603 (2014).
- [31] Ren, H. *et al.* Two-dimensional optomechanical crystal cavity with high quantum cooperativity. *Nature Communications* **11**, 3373 (2020).
- [32] Madiot, G., Albrechtsen, M., Stobbe, S., Sotomayor-Torres, C. M. & Arregui, G. Multimode optomechanics with a two-dimensional optomechanical crystal. *APL Photonics* **8**, 116107 (2023).
- [33] Chiappina, P. *et al.* Design of an ultra-low mode volume piezo-optomechanical quantum transducer. *Optics Express* **31**, 22914 (2023).
- [34] Weaver, M. J. *et al.* An integrated microwave-to-optics interface for scalable quantum computing. *Nature Nanotechnology* **19**, 166–172 (2024).
- [35] Krastanov, S. *et al.* Optically Heralded Entanglement of Superconducting Systems in Quantum Networks. *Physical Review Letters* **127**, 040503 (2021).
- [36] Zhong, C. *et al.* Proposal for Heralded Generation and Detection of Entangled Microwave–Optical-Photon Pairs. *Physical Review Letters* **124**, 010511 (2020).
- [37] Zhong, C., Han, X., Tang, H. X. & Jiang, L. Entanglement of microwave-optical modes in a strongly coupled electro-optomechanical system. *Physical Review A* **101**, 032345 (2020).
- [38] Aram, M. H. & Khorasani, S. Optomechanical coupling strength in various triangular phononic crystal slab cavities. *Journal of the Optical Society of America B* **35**, 1390 (2018).
- [39] Hopcroft, M. A., Nix, W. D. & Kenny, T. W. What is the Young’s Modulus of Silicon? *Journal of Microelectromechanical Systems* **19**, 229–238 (2010).
- [40] Primo, A. G. *et al.* Quasinormal-Mode Perturbation Theory for Dissipative and Dispersive Optomechanics. *Physical Review Letters* **125**, 233601 (2020).
- [41] Aspelmeyer, M., Kippenberg, T. J. & Marquardt, F. Cavity optomechanics. *Reviews of Modern Physics* **86**, 1391–1452 (2014).
- [42] Xu, M. *et al.* Radiative Cooling of a Superconducting Resonator. *Physical Review Letters* **124**, 033602 (2020).
- [43] Meenehan, S. M. *et al.* Silicon optomechanical crystal resonator at millikelvin temperatures. *Physical Review A* **90**, 011803 (2014).
- [44] Safavi-Naeini, A. H. *et al.* Laser noise in cavity-optomechanical cooling and thermometry. *New Journal of Physics* **15**, 035007 (2013).
- [45] Primo, A. G. *et al.* Dissipative optomechanics in high-frequency nanomechanical resonators. *Nature Communications* **14**, 5793 (2023).
- [46] Chan, J. *et al.* Laser cooling of a nanomechanical oscillator into its quantum ground state. *Nature* **478**, 89–92 (2011).
- [47] Safavi-Naeini, A. H. *et al.* Electromagnetically induced transparency and slow light with optomechanics. *Nature* **472**, 69–73 (2011).
- [48] Gröblacher, S., Hammerer, K., Vanner, M. R. & Aspelmeyer, M. Observation of strong coupling between a micromechanical resonator and an optical cavity field. *Nature* **460**, 724–727 (2009).
- [49] Fiaschi, N. *et al.* Optomechanical quantum teleportation. *Nature Photonics* **15**, 817–821 (2021).
- [50] Wallucks, A., Marinković, I., Hensen, B., Stockill, R. & Gröblacher, S. A quantum memory at telecom wavelengths. *Nature Physics* **16**, 772–777 (2020).
- [51] MacCabe, G. S. *et al.* Nano-acoustic resonator with ultralong phonon lifetime. *Science* **370**, 840–843 (2020).
- [52] Asano, T., Ochi, Y., Takahashi, Y., Kishimoto, K. & Noda, S. Photonic crystal nanocavity with a Q factor exceeding eleven million. *Optics Express* **25**, 1769–1777 (2017).
- [53] Alegre, T. P. M., Safavi-Naeini, A., Winger, M. & Painter, O. Quasi-two-dimensional optomechanical crystals with a complete phononic bandgap. *Optics Express*

19, 5658–5669 (2011).

- [54] Safavi-Naeini, A. H. & Painter, O. Design of optomechanical cavities and waveguides on a simultaneous bandgap phononic-photon crystal slab. *Optics Express* **18**, 14926–14943 (2010).

METHODS

A. Fabrication

We start device fabrication by using electron-beam lithography (Raith EBPG 5200+, 100 kV) to pattern the OMCs on a silicon-on-insulator (SOI) chip (220 nm thick silicon device layer, 3 μm thick buried oxide, 725 μm silicon handle, Shin-Etsu, $> 3 \text{ k}\Omega \cdot \text{cm}$) with AR-P 62.00 e-beam resist. Next, we do an inductively coupled plasma (ICP) - reactive ion etch (RIE) of the silicon using HBr-based chemistry. The chip is then diced to allow optical fiber access to the coupling waveguide. The substrate is subsequently cleaned in a piranha solution (96 % sulfuric acid and 30 % hydrogen peroxide - 3:1) to remove any organic residue. Finally, the structure is released in 50 % hydrofluoric acid (HF) for 2.5 min. Immediately before loading the device into the cryostat we strip the native oxide with a 2 % HF dip.

B. Heating model

The ground-state cooling data shown in Fig. 2d is fitted using a model accounting for the presence of pump-induced heating through

$$n_m(n_c) = \frac{1}{1+C} \left(n_{\text{th}}^0 + \frac{\alpha_{\text{sat}}}{1+\beta_{\text{sat}}n_c} n_c + \alpha_{\text{lin}} n_c \right), \quad (1)$$

where both saturable and linear absorption terms are used to phenomenologically describe the increase in the temperature of the mechanical mode’s thermal bath. The fit results are $\alpha_{\text{sat}} = 0.324$, $\beta_{\text{sat}} = 0.019$, and $\alpha_{\text{lin}} = 0.003$, indicating an increase in the bath’s temperature to approximately 7 K (from an initial $T = 3 \text{ K}$) at $n_c \approx 5000$.

DATA AVAILABILITY

The data that support the findings of this study are available from the corresponding author upon reasonable request.

ACKNOWLEDGMENT

The authors thank O. A. Hitchcock, M. P. Maksymowych, R. G. Gruenke and K. K. S. Multani for

helpful discussions and technical assistance. This work was primarily supported by the US Army Research Office (ARO)/Laboratory for Physical Sciences (LPS) Modular Quantum Gates (ModQ) program (Grant No. W911NF-23-1-0254). Some of this work was funded by the US Department of Energy through grant no. DE-AC02-76SF00515 and via the Q-NEXT Center, and by the National Science Foundation CAREER award no. ECCS-1941826. We also thank Amazon Web Services Inc. for their financial support. Device fabrication was performed at the Stanford Nano Shared Facilities (SNSF) and the Stanford Nanofabrication Facility (SNF), supported by NSF award ECCS-2026822. A.G.P and T.P.M.A. acknowledge the São Paulo Research Foundation (FAPESP) through grants 2023/00058-0, 19/09738-9, 18/15577-5, 18/25339-4, and Coordenação de Aperfeiçoamento de Pessoal de Nível Superior - Brasil (CAPES) (Finance Code 001). S.G. acknowledges the Knut and Alice Wallenberg foundation (grant no. KAW 2021-0341).

COMPETING INTERESTS

A.H.S.-N. is an Amazon Scholar. The other authors declare no competing interests.

SUPPLEMENTARY INFORMATION

Supplementary Note 1. MEASURED DEVICE PARAMETERS

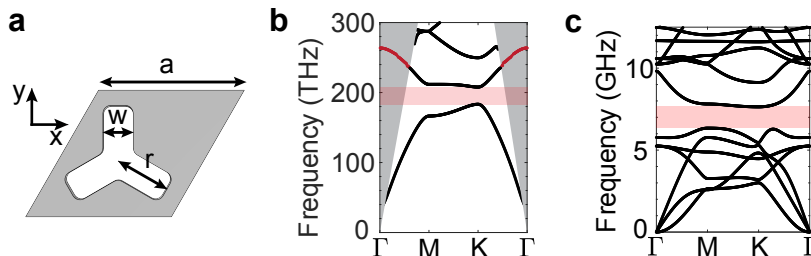
The data presented in this work was acquired from two devices from different fabrication runs. Device A (D120) was measured at 3 K after Device B's (D122) thermometry measurements at less than 10 mK were cut short due to infrastructure difficulties.

Supplementary Data Table I. **Device parameters**

Parameter	Device A (D120)	Device B (D122)	Method
$\omega_o/2\pi$	191.7 THz	193.9 THz	Laser wavelength sweep
$\kappa_o/2\pi$	0.8 GHz	1.1 GHz	Laser wavelength sweep
$\kappa_{o,e}/2\pi$	288 MHz	196 MHz	OMIT
$g_o/2\pi$	860 kHz	889 kHz	Mechanical response ($\Delta = \omega_m$)
$\omega_m/2\pi$	7.436 GHz	7.259 GHz	OMIT
$\gamma_i/2\pi$	206 kHz	715 kHz	Mechanical response ($\Delta = \omega_m$)
Fiber to chip coupling efficiency	43.0 %	51.1 %	Power meter

Supplementary Note 2. OPTOMECHANICAL CRYSTAL DESIGN

To design the optomechanical shield, we consider multiple factors. It should simultaneously have a large optical bandgap at telecom frequencies and a complete phononic bandgap at frequencies commonly used for superconducting qubits. Ideally, we would also like to have the volume of the unit cell be filled with as much silicon as possible, i.e. we would like a large filling factor. This is to help with thermalization and reduce the number of surfaces that can lead to optical scattering. While the snowflake unit cell [54] fulfills most of these requirements, OMCs using the snowflake have so far been restricted to mechanical frequencies of ~ 10 GHz [31]. This makes it challenging to design and fabricate a transducer that efficiently couples the breathing mode of such an OMC to superconducting circuits. This is mainly due to the smaller required feature sizes of a piezoelectric transducer at higher frequencies. To address this issue, we use the boomerang unit cell [38] which supports a lower frequency acoustic bandgap than the snowflake at the cost of a smaller relative photonic and phononic bandgap. A schematic of the unit cell is shown in Supplementary Figure 1a. Finite-element method (FEM) simulations with periodic boundary conditions (Supplementary Figure 1b) show that for 220 nm thick silicon and $(a, r, w) = (448 \text{ nm}, 172 \text{ nm}, 93 \text{ nm})$ the optomechanical shield supports an optical pseudo-bandgap for TE-like guided optical waves. This bandgap spans the telecom frequencies 183 – 208 THz and, importantly, does not close inside the light cone [54]. Additionally, FEM simulations assuming mechanically-isotropic silicon (Supplementary Figure 1c) reveal a 1.30 GHz-wide complete acoustic bandgap centered at 6.99 GHz. The filling factor of the boomerang unit cell is 74.5 %, 15 % larger than the 64.1 % filling factor of the snowflake unit cell.



Supplementary Figure 1. **Optomechanical shield design.** **a**, Boomerang unit cell schematic. **b**, Photonic band structure for the even parity modes. The bandgap is highlighted in pink and the light cone in grey. Notice how the bands for the leaky modes (red) inside the light cone do not close the bandgap. **c**, Phononic band structure. The bandgap is highlighted in pink.

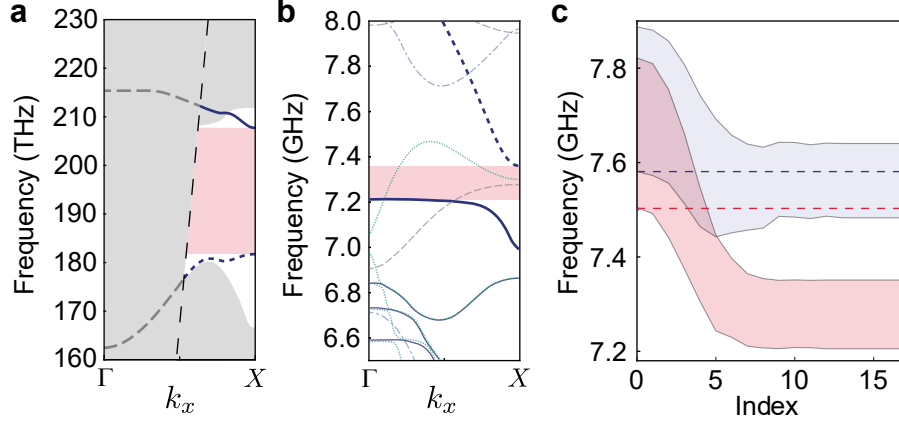
As described in the main text, the dagger parameters in each waveguide unit cell are adiabatically transitioned from the center defect (index 0) to the most external cell (index N , for an OMC with $2N + 1$ unit cells). The function that parametrizes these variations is given by

$$v_n = v_N - (v_N - v_0) 2^{-\left(\frac{n}{\delta_x}\right)^M}, \quad (2)$$

where v_n is a given parameter of the dagger (d or h) for the n -th unit cell. The parameters M and δ_x control how smooth the variation in v is as a function of n and how many waveguide cells will effectively make the transition from v_0 to v_N .

A FEM simulation of the waveguide unit cell shown in Fig. 1a is performed assuming Floquet periodic conditions. It shows the existence of an incomplete (complete) bandgap in the photonic (phononic) domains, as shown in red in Supplementary Figure 2a (b). Importantly, the acoustic bands inside the bandgap display different symmetries than our mode of interest minimizing their coupling, as easily verified through the absence of anti-crossings in the red-shaded area.

Supplementary Figure 2c shows the bandgap – obtained from the same simulations described above – as a function of the unit cell index. Although the mechanical frequency falls outside the bandgap after index 4 in device B, it keeps a high mechanical quality factor in simulations $Q_m > 5 \times 10^6$, whereas device A has a $Q_m > 10^9$. In practice, fabrication imperfections allied to the small acoustic bandgaps give rise to a radiation-limited measured Q_m . Adding a surrounding array of rectangular phononic shields could boost our Q_m , at the cost of potentially worse thermal anchoring to the substrate, becoming a less favorable configuration for transduction applications.



Supplementary Figure 2. **Effective waveguide band structure.** FEM simulations of the waveguide unit cell of device B displaying its **a**, photonic and **b**, acoustic band structures. Solid dark blue bands represent modes with symmetry groups where $\sigma_z = \sigma_y = 1$, meaning they are symmetric for reflections across the y and z axes. Dotted green curves are $\sigma_z = -\sigma_y = 1$, dashed grey curves are $\sigma_z = \sigma_y = -1$, and light blue dash-dotted curves denote $-\sigma_z = \sigma_y = 1$. Dark blue dashed curves indicate the bands giving rise to the confined optical and acoustic modes. Results for device A are qualitatively similar. **c**, Mechanical bandgap as a function of cell index. The blue (red) shaded region shows results for device A (B).

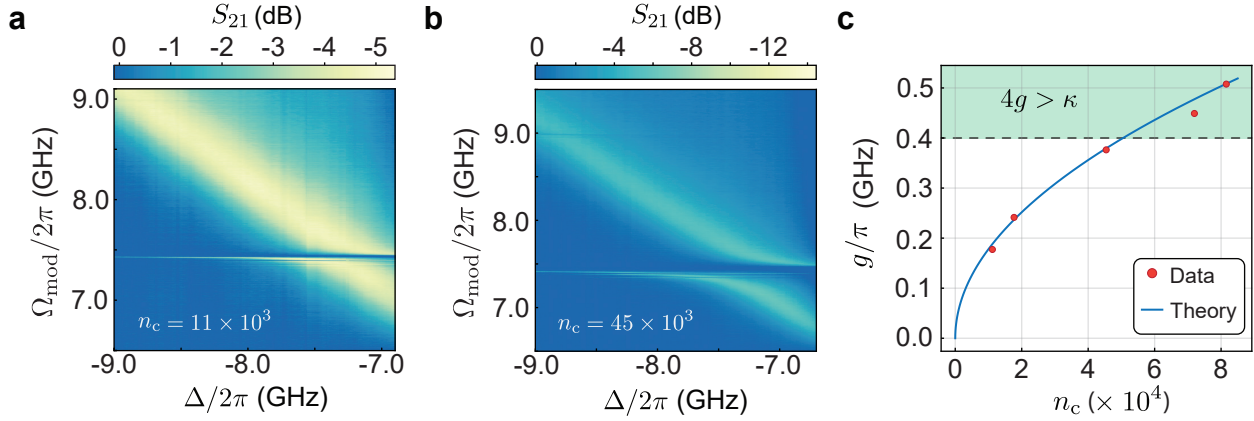
All design parameters of Device A and B parameters are provided in Table II.

Supplementary Data Table II. **Design parameters**

Parameter	Device A (D120)	Device B (D122)
a	448 nm	448 nm
w	92 nm	93 nm
r	167 nm	172 nm
d_0	70 nm	76 nm
h_0	194.5 nm	196.9 nm
d_{17}	122 nm	123 nm
h_{17}	217.6 nm	231 nm
u_y	356 nm	359 nm
fillet radius	25 nm	25 nm
δ_x	4.2	3.68
M	2.55	2.55

Supplementary Note 3. ONSET OF THE STRONG COUPLING REGIME

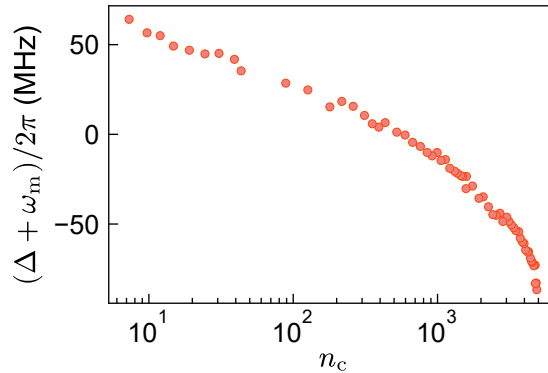
Additional optomechanically-induced transparency (OMIT) experiments were performed below and above the threshold for the strong coupling regime, as exemplified in Supplementary Figure 3a and b. The splitting resulting from OMIT – a direct measurement of g/π – agrees well with predictions assuming the independently measured g_0 from cooling and heating experiments described in the main text, as displayed in Supplementary Figure 3c.



Supplementary Figure 3. **Onset of the strong coupling regime.** Optomechanically-induced transparency measurement as a function of laser-cavity detuning Δ for **a**, $n_c = 11 \times 10^3$ and **b**, $n_c = 45 \times 10^3$. **c**, Mode splitting due to OMIT as a function of n_c . The green-shaded area denotes the optomechanical strong coupling regime. The theory trace was obtained using the measured g_0 from dynamical backaction experiments shown in the main text.

Supplementary Note 4. OPTICAL STABILITY AT 3 K

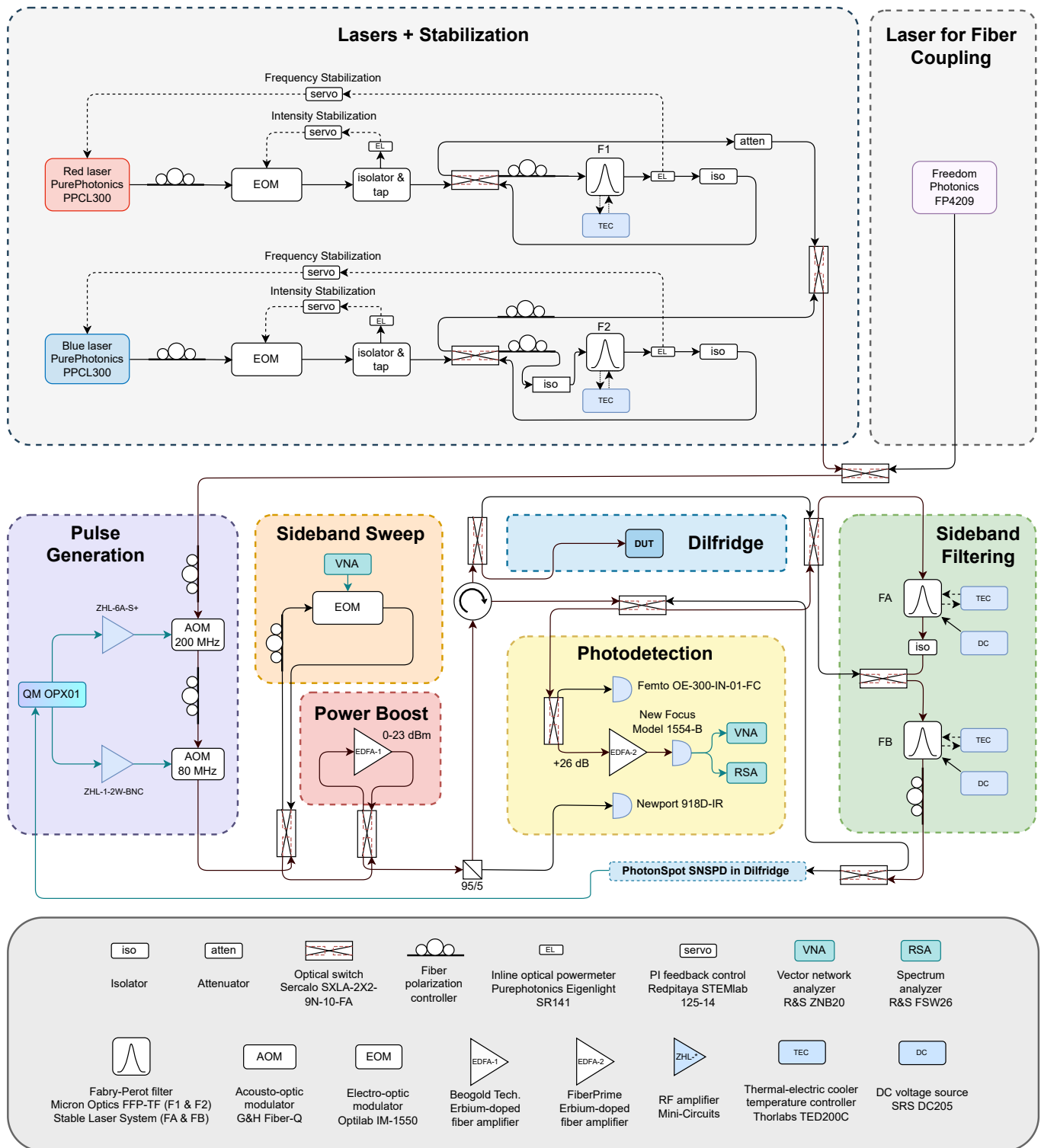
We intensity modulate a pump laser ($\Delta = -\omega_m$) at a frequency Ω_{mod} using an electro-optical intensity modulator and a vector network analyzer. The reflected signal from the device is measured on a high-speed photodiode. The beating signal between the carrier and sideband contains information about the optical mode of the device. We track the detuning (Supplementary Figure 4) between the unlocked laser and the location of the optical mode, depending on the incoming laser power. We observe shifts < 150 MHz even for cavity occupations up to $n_c \approx 5000$.



Supplementary Figure 4. **Optical Power stability.** Frequency shift of the optical mode versus cavity photon occupation n_c measured using coherent spectroscopy of the optical mode.

Supplementary Note 5. MEASUREMENT SETUP

A schematic of the full experimental setup used in the sideband asymmetry, ground state cooling, and optomechanical strong coupling is provided in Supplementary Figure 5. Two tunable diode lasers (PurePhotonics PPCL300) are first intensity-stabilized with electro-optic modulators (EOMs), and then frequency-stabilized using temperature-stabilized fiber Fabry-Pérot filters (F1 and F2). A fast wavelength-scanning laser (Freedom Photonics FP4209) assists with fiber-to-chip coupling in the dilution refrigerator. Two acousto-optic modulators (AOMs) in-series are simultaneously pulsed, utilizing a Quantum Machine OPX, to generate the optical pump pulse with a high on-off ratio (> 90 dB) for the pulsed operation. On the other hand, sending a constant signal to the AOMs enables continuous-wave (CW) operation. A pair of narrow-band Fabry-Pérot cavities (FA and FB), with bandwidth ≈ 15 MHz, suppress the pump photons with a joint suppression of > 90 dB with respect to the sideband photons. Multiple MEMS optical switches route light to various segments of the setup: an EOM to generate and sweep sidebands (used for OMIT measurements, locking filter cavities FA and FB, calibrating the cooling measurement), an erbium-doped fiber amplifier (EDFA) to boost input power to the device (for the strong-coupling measurement), filter cavities FA and FB to suppress the pump before single photon detection (Photonspot, used for pulsed asymmetry measurements), and a high-speed photodetector (for OMIT, cooling, and strong-coupling measurements).



Supplementary Figure 5. **Measurement Setup.** Diagram representing the full optical setup used in the pulsed and CW measurements.